THE UNIVERSITY *of* EDINBURGH

Edinburgh Research Explorer

Graph Signal Processing-Based Imaging for Synthetic Aperture Radar

OPEN ACCESS

Graph Signal Processing Based Imaging for Synthetic Aperture Radar

Shahzad Gishkori and Bernard Mulgrew

Abstract—In this paper, we propose graph signal processing based imaging for synthetic aperture radar (SAR). Our method provides improved denoising and resolution enhancing capabilities, along with a reduction in computational complexity, by exploiting the concept of extended neighbourhood in SAR images. We present a modified version of fused least absolute shrinkage and selection operator (LASSO) to cater for graph structure of the SAR image. It can also accommodate the compressed sensing framework. We solve the optimisation problem via alternating direction method of multipliers. Experimental results on a backhoe target corroborate the validity of our proposed method.

Index Terms—Graph Signal Processing, SAR imaging, Fused LASSO

I. INTRODUCTION

Synthetic aperture radar (SAR) [1]–[3] is known to provide high-resolution radar images via its different modes of operation. A large body of work is available to enhance the quality of SAR images in terms of denoising and super-resolution (see [4] and its references). Most of the proposed techniques have been borrowed from optical imaging. Nonetheless, enhancing the quality of a SAR image is a challenging task. One of the reasons is the disparity between range and cross-range resolutions, with latter generally being lower than the former. This leads to an image spread over an irregular grid. Secondly, radar returns from a target scene are heavily dependent upon the aspect angles and/or position of the radar. Small variations in the aspect angles or position can produce completely different reflectivity pattern which results in a nonuniform image. This can be challenging in imaging extended objects where adjacent reflective points on the object may produce drastically different reflectivities. Thus, a straightforward application of general imaging techniques on SAR provides limited gains. However, one of the qualities of SAR, that differentiates it from other imaging sensors, is the availability of precise ranging information. Exploiting this extra information can potentially enhance the quality of a SAR image.

Graph signal processing (GSP) [5]–[7] has recently been proposed as a technique which processes signals lying on specific data structures defined by the graphs (see [8] for an earlier context). This essentially means that all elements/samples of the signal form vertices on a graph and the edge weights connecting these vertices provide a measure of similarity between

them. Thus, a graph signal can assume any irregularity of structure and it can get processed accordingly. In our case, the disparity between range resolution and cross-range resolution gives rise to an irregular grid structure of a SAR image, which is further complicated by overlapping grids from different aspect angles. Therefore, substantial gains can be obtained by applying the GSP techniques to SAR imaging.

Fused least absolute shrinkage and selection operator (FLASSO) [9] is known to provide element-wise sparsity as well as smoothness. We have recently used FLASSO in [10] for SAR imaging of an automotive scene for improved azimuth resolution. In FLASSO, smoothness is achieved by total variation (TV) [11]. TV is an edge-preserving norm and it has been at the forefront of image denoising for many years. The basic idea is to minimise the difference between consecutive image pixels which results in noise reduction and feature enhancement. TV can be related to a graph with unit edge weights between adjacent pixels only. Recently, some works have advocated the use of nonlocal neighbours, i.e., a nonlocal TV (NLTV), for improved results, see, e.g., [12]–[14] for general images and [15]–[17] for SAR imagery. Nonlocal neighbourhood is defined in terms of similarity of patches centred around different pixels over the complete image. The edge weights are then a function of a Euclidean distance between the patches (in terms of pixel intensities) of a coarse estimate of the reconstructed image. NLTV provides good results. However, searching for neighbours and computing edge weights is a computationally intensive process. Nonetheless, in NLTV, apart from the computational complexity issues of searching for nonlocal neighbours, edge weights are still dependent upon pixel intensities. Given the nonuniform reflectivity pattern of SAR images, generating edge weights based on pixel intensities can provide only limited gains.

Contributions. In this paper, we propose extended neighbourhood (EN) for SAR images. It essentially comprises of all the pixels within a certain spatial proximity. Thus, the weight function reflects the actual ranges and avoids the exhaustive search for intensity based neighbours, causing a drastic reduction in computational complexity. The rationale is that, for an extended object, there is a high probability of finding similar scatterers in close proximity. Also, given the availability of precise ranging information in SAR images, such an approach can be quite effective. In the light of above, we combine the concept of GSP with EN and reformulate the FLASSO cost function as graph fused LASSO with extended neighbourhood total variation (GFL-ENTV). We solve our optimisation problem via alternating direction method of multipliers (ADMM) [18], [19], which enjoys the benefits of
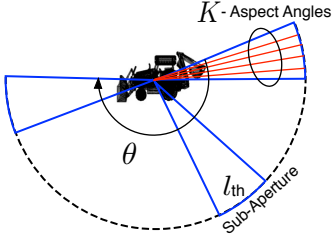
Fig. 1: Spot-SAR Measurement Schematic

parallelisation and fast convergence. Our method can easily accommodate the compressed sensing (CS) framework [20], [21] as well. This is particularly useful in the case of insufficient SAR measurements. Therefore, we provide a composite signal model, accordingly. Our proposed approach results in enhanced spatial resolution and improved SAR imaging. For a fair comparison, we cast NLTV in GFL framework, i.e., GFL-NLTV. We provide experimental results to prove the effectiveness of our proposed method.

Notations. Matrices are in upper case bold while column vectors are in lower case bold, $(\cdot)^T$ denotes transpose whereas $(\cdot)^H$ denotes Hermitian, $[\mathbf{a}]_i$ is the ith element of $\mathbf{a}$ and $[\mathbf{A}]_{ij}$ is the ijth element of $\mathbf{A}$, $\hat{\mathbf{a}}$ is the estimate of $\mathbf{a}$, $\triangleq$ defines an entity, $|\mathcal{A}|$ denotes the cardinality of set $\mathcal{A}$, and the ℓ_p-norm is denoted as $||\mathbf{a}||_p = (\sum_{i=1}^{N} |[\mathbf{a}]_i|^p)^{1/p}$.

II. SIGNAL MODEL

In this paper, we focus on spotlight mode SAR (Spot-SAR). However, our proposed techniques are applicable for other modes as well. In Spot-SAR, the target scene is illuminated from different aspect angles θ, which form the synthetic aperture. Depending on the range of aspect angles, synthetic aperture can be narrow- or wide-angle. In contrast to the wide-angle, a narrow-angle synthetic aperture assumes that the target reflectivity is isotropic over all aspect angles. However, a wide-angle synthetic aperture can be modelled to consist of many narrow-angle synthetic apertures, named as sub-apertures. Figure 1 shows the measurement schematic of such a wide-angle Spot-SAR. The received signal (after some post-processing) can be modelled as a spatial Fourier transform of the target field reflectivity (see [4] and its references), i.e.,

$$r(\gamma_m, \theta_k^l) = \sum_{n=1}^{N} s(x_n, y_n; \theta_k^l) \exp\left(-j2\pi\gamma_m \phi_{n,k}^l\right) + \nu(\gamma_m, \theta_k^l) \tag{1}$$

where $\phi_{n,k}^l \triangleq 2(x_n \cos\theta_k^l + y_n \sin\theta_k^l)/c$, γ_m is the mth spatial frequency, for $m = 1, \cdots, M$, θ_k^l is the kth aspect angle, for $k = 1, \cdots, K$, within lth sub-aperture, for $l = 1, \cdots, L$, $s(x_n, y_n; \theta_k^l)$ is the reflectivity function of the nth spatial location (x_n, y_n) in a Cartesian coordinate system, conditioned on θ_k^l, for $n = 1, \cdots, N$ and $\nu(\gamma_m, \theta_k^l)$ is the model noise corresponding to γ_m and θ_k^l. Now, we can write (1) in the following discrete form.

$$\mathbf{r}_k^l = \mathbf{\Phi}_k^l \mathbf{s}_k^l + \boldsymbol{\nu}_k^l \tag{2}$$

where $\mathbf{r}_k^l$ is an $M \times 1$ vector of samples of $r(\gamma_m, \theta_k^l)$, $\mathbf{\Phi}_k^l$ is an $M \times N$ matrix of the samples of $\exp(-j2\pi\gamma_m\phi_{n,k}^l)$, $\mathbf{s}_k^l$

is an $N \times 1$ vector of samples of field reflectivity function $s(x_n, y_n; \theta_k^l)$ and $\boldsymbol{\nu}_k^l$ is an $M \times 1$ vector of samples of noise $\nu(\gamma_m, \theta_k^l)$. Note, all the aforementioned samples are taken for a given θ_k^l. Now, a composite model of (2) can be written as

$$\mathbf{y}^l = \mathbf{\Theta}^l \mathbf{s}^l + \mathbf{n}^l \tag{3}$$

where $\mathbf{y}^l \triangleq \mathbf{\Psi}[\mathbf{r}_1^{l\,T}, \cdots, \mathbf{r}_K^{l\,T}]^T$ is a $KJ \times 1$ vector, $\mathbf{\Theta}^l \triangleq \mathbf{\Psi}[\mathbf{\Phi}_1^{l\,T}, \cdots, \mathbf{\Phi}_K^{l\,T}]^T$ is a $KJ \times N$ matrix, $\mathbf{n}^l \triangleq \mathbf{\Psi}[\boldsymbol{\nu}_1^{l\,T}, \cdots, \boldsymbol{\nu}_K^{l\,T}]^T$ is a $KJ \times 1$ vector and $\mathbf{\Psi}$ is a $KJ \times KM$ random selection matrix [22], with $J \leq M$. Note, the above model is valid for narrow-angle sub-apertures, i.e., K is spread over few degrees of angles, under the assumption that the reflectivity function $s(x_n, y_n; \theta_k^l)$ remains isotropic over all k for a given l. Thus, $\mathbf{s}^l = \mathbf{s}_k^l$, $\forall k$. After obtaining an estimate of $\mathbf{s}^l$, $\forall l$, in (3), a composite response to the field reflectivity of the nth spatial location (x_n, y_n) can be obtained as

$$[\tilde{\mathbf{s}}]_n = \max_l |[\hat{\mathbf{s}}^l]_n|^2 \tag{4}$$

for $n = 1, \cdots, N$, which has the interpretation of a generalised likelihood ratio test (GLRT) over the sub-apertures (see [23] for more details). We solve (3) for each lth sub-aperture and drop the superscript depicting sub-aperture in subsequent sections, for notational simplicity. Note, instead of (3), some authors, e.g., [24], [25] have also advocated a 2-D measurement model. Such models may also be employed in connection with our proposed method.

III. GSP BASED SAR IMAGING

A graph can be defined as a tuple $\mathcal{G} \triangleq (\mathcal{V}, w)$, where $\mathcal{V} \triangleq \{v_1, \cdots, v_N\}$ is a set of N vertices and w is a weight map between each pair of elements in $\mathcal{V}$, i.e., $w(v_n, v_{n'}) \in \mathbb{R}_+$, where $v_n, v_{n'} \in \mathcal{V}$. Generally, $w(v_n, v_n) = 0$, i.e., no self-loops. Note, in this paper, we consider undirected graphs, i.e., $w(v_n, v_{n'}) = w(v_{n'}, v_n)$. Two vertices are connected to each other if their respective weight map is nonzero. For an nth vertex, all its connected vertices define its neighbourhood $\mathcal{N}_n$, i.e., $\mathcal{N}_n \triangleq \{v_{n'} \in \mathcal{V} : w(v_n, v_{n'}) \neq 0\}$. The weight map w can be described in the form of an $N \times N$ adjacency matrix $\mathbf{W}$, where $[\mathbf{W}]_{nn'} = w(v_n, v_{n'})$. An $N \times N$ degree matrix $\mathbf{D}$ is defined as, $[\mathbf{D}]_{nn} = \sum_{n'} w(v_n, v_{n'})$, which is a diagonal matrix. Then, the (combinatorial) graph Laplacian is defined as, $\mathbf{L} = \mathbf{D} - \mathbf{W}$.

As explained in Section I, radar signals can be processed under the GSP framework. Thus, a radar graph signal $\mathbf{s}$ can be defined as a map from graph vertices to complex-valued signal samples, i.e., $\mathbf{s} : \mathcal{V} \to \mathbb{C}$, $v_n \mapsto [\mathbf{s}]_n$. Transforming a graph signal by the graph Laplacian generates weighted smoothing of the graph signal, i.e.,

$$[\mathbf{Ls}]_n = \sum_{[\mathbf{s}]_{n'} \in \mathcal{N}_n} [\mathbf{W}]_{nn'} ([\mathbf{s}]_n - [\mathbf{s}]_{n'}) \tag{5}$$

which shows that the GSP framework enables processing variations of a signal spread over any kind of graph structure, as determined by $\mathcal{N}_n$. Now, in the context of GSP, our proposed GFL optimisation problem can be written as

$$\hat{\mathbf{s}} = \arg\min_{\mathbf{s}} \frac{1}{2}\|\mathbf{y} - \mathbf{\Theta s}\|_2^2 + \lambda_e\|\mathbf{s}\|_1^1 + \lambda_f\|\mathbf{\Lambda s}\|_1^1 \tag{6}$$

where $\lambda_e, \lambda_f > 0$ are penalty parameters for element-wise sparsity and graph fusion[1], respectively, and $\mathbf{\Lambda}$ is the $\sum_{n=1}^{N} |\mathcal{N}_n| \times N$ graph difference matrix defined as $\mathbf{\Lambda} \triangleq [\mathbf{\Lambda}_1^T, \cdots, \mathbf{\Lambda}_N^T]^T$, where $\mathbf{\Lambda}_n$ is an $|\mathcal{N}_n| \times N$ matrix such that

$$[\mathbf{\Lambda}_n]_{ij} = \begin{cases} +[\mathbf{W}]_{n\{\mathcal{N}_n\}_i} & j = n \\ -[\mathbf{W}]_{n\{\mathcal{N}_n\}_i} & j = \{\mathcal{N}_n\}_i \\ 0 & \text{otherwise} \end{cases} \quad (7)$$

where (with some abuse of notation) $\{\mathcal{N}_n\}_i$ denotes the vertex index of the ith element in set $\mathcal{N}_n$, for $i = 1, \cdots, |\mathcal{N}_n|$, and $j = 1, \cdots, N$. From (7), we can see that $\mathbf{\Lambda}_n$ is in fact a reshaped form of the nonzero elements of the nth row of $\mathbf{L}$, i.e., $[\mathbf{L}]_{n:} \longrightarrow \mathbf{\Lambda}_n$. Thus, the fusion part of the GFL can be expanded as

$$\|\mathbf{\Lambda}\mathbf{s}\|_1^1 = \sum_{n=1}^{N} \sum_{[\mathbf{s}]_{n'} \in \mathcal{N}_n} [\mathbf{W}]_{nn'} \|([\mathbf{s}]_n - [\mathbf{s}]_{n'})\|_1^1 \quad (8)$$

which creates parsimony over the weighted absolute difference of the neighbouring spatial samples. Thus, GFL encourages sparsity both in the individual elements of $\mathbf{s}$ as well as in neighbouring pairs of the elements of $\mathbf{s}$. This problem formulation results in increased resolution of the target scene as well as improved imaging of the extended targets. We solve the GFL problem via ADMM. Thus, (6) can be re-written as

$$[\hat{\mathbf{s}}, \hat{\mathbf{u}}, \hat{\mathbf{z}}] = \arg\min_{\mathbf{s},\mathbf{u},\mathbf{z}} \frac{1}{2}\|\mathbf{y} - \mathbf{\Theta}\mathbf{s}\|_2^2 + \lambda_e\|\mathbf{u}\|_1^1 + \lambda_f\|\mathbf{z}\|_1^1$$
$$\text{s.t.} \quad \mathbf{u} = \mathbf{s}, \quad \mathbf{z} = \mathbf{\Lambda}\mathbf{s} \quad (9)$$

where $\mathbf{u}$ and $\mathbf{z}$ are $N \times 1$ and $\sum_{n=1}^{N} |\mathcal{N}_n| \times 1$ auxiliary variables, respectively. Now, the cost function in (9) can be written in the following unconstrained form.

$$\mathcal{L}(\mathbf{s}, \mathbf{u}, \mathbf{z}, \boldsymbol{\rho}_u, \boldsymbol{\rho}_z) = \frac{1}{2}\|\mathbf{y} - \mathbf{\Theta}\mathbf{s}\|_2^2 + \lambda_e\|\mathbf{u}\|_1^1 + \lambda_f\|\mathbf{z}\|_1^1 +$$
$$\boldsymbol{\rho}_u^H(\mathbf{u} - \mathbf{s}) + \frac{c_u}{2}\|\mathbf{u} - \mathbf{s}\|_2^2 + \boldsymbol{\rho}_z^H(\mathbf{z} - \mathbf{\Lambda}\mathbf{s}) + \frac{c_z}{2}\|\mathbf{z} - \mathbf{\Lambda}\mathbf{s}\|_2^2 \quad (10)$$

where $\boldsymbol{\rho}_u$ and $\boldsymbol{\rho}_z$ are Lagrange multipliers, and c_u and c_z are positive constants. An iterative solution of (9), for the tth iteration can be obtained by minimising (10) over $\mathbf{s}$, $\mathbf{u}$ and $\mathbf{z}$, one-at-a-time, while keeping other variables fixed. Thus, a closed-from estimate of $\mathbf{s}$ can be written as

$$\hat{\mathbf{s}}^{[t]} = \left(\mathbf{\Theta}^H\mathbf{\Theta} + c_u\mathbf{I} + c_z\mathbf{\Lambda}^T\mathbf{\Lambda}\right)^{-1}$$
$$\times \left(\mathbf{\Theta}^H\mathbf{y} + \hat{\boldsymbol{\rho}}_u^{[t-1]} + c_u\hat{\mathbf{u}}^{[t-1]} + \mathbf{\Lambda}^T\hat{\boldsymbol{\rho}}_z^{[t-1]} + c_z\mathbf{\Lambda}^T\hat{\mathbf{z}}^{[t-1]}\right). \quad (11)$$

Note, the matrix inversion in (11) does not depend on iteration index t. Therefore, its off-line calculation can save substantial amount of computation. An estimate of $\mathbf{u}$ can be written as

$$\hat{\mathbf{u}}^{[t]} = \eta\left(\left[\hat{\mathbf{s}}^{[t-1]} - \frac{\hat{\boldsymbol{\rho}}_u^{[t-1]}}{c_u}\right], \frac{\lambda_e}{c_u}\right) \quad (12)$$

where $\eta(\mathbf{s}, \lambda) = \text{sign}(\mathbf{s})(|\mathbf{s}| - \lambda)_+$, with $\text{sign}([\mathbf{s}]_n) \triangleq [\mathbf{s}]_n/|[\mathbf{s}]_n|$, and an estimate of $\mathbf{z}$ can be written as

$$\hat{\mathbf{z}}^{[t]} = \eta\left(\left[\mathbf{\Lambda}\hat{\mathbf{s}}^{[t-1]} - \frac{\hat{\boldsymbol{\rho}}_z^{[t-1]}}{c_z}\right], \frac{\lambda_f}{c_z}\right). \quad (13)$$

The Lagrange multipliers can be updated as

$$\hat{\boldsymbol{\rho}}_u^{[t]} = \hat{\boldsymbol{\rho}}_u^{[t-1]} + c_u(\hat{\mathbf{u}}^{[t]} - \hat{\mathbf{s}}^{[t]}) \quad (14)$$
$$\hat{\boldsymbol{\rho}}_z^{[t]} = \hat{\boldsymbol{\rho}}_z^{[t-1]} + c_z(\hat{\mathbf{z}}^{[t]} - \mathbf{\Lambda}\hat{\mathbf{s}}^{[t]}). \quad (15)$$

Now, the weights in the adjacency matrix are generally obtained from a Gaussian kernel [5], i.e.,

$$[\mathbf{W}]_{nn'} = \begin{cases} \exp\left(-\frac{\Delta_{nn'}^2}{2\sigma^2}\right) & \text{if } \Delta_{nn'} \leq D \\ 0 & \text{otherwise} \end{cases} \quad (16)$$

where σ^2 is the variance and $\Delta_{nn'}$ is a function of physical or feature space distances between nth and n'th vertices. In NLTV, $\Delta_{nn'}$ is the Euclidean distance between image patches of certain dimension, centred around the neighbouring vertices. Generally, a coarse estimate of the reconstructed image is used to find these weights. It is defined as

$$\Delta_{nn'}^{\text{NL}} \triangleq \left\|\hat{\mathbf{s}}_{\mathcal{I}_n} - \hat{\mathbf{s}}_{\mathcal{I}_{n'}}\right\|_2 \quad (17)$$

where $\mathcal{I}_n$ is a set of indices corresponding to the pixels in image patch centred around vertex $[\mathbf{s}]_n$. Thus, $\hat{\mathbf{s}}_{\mathcal{I}_n}$ contains elements of $\hat{\mathbf{s}}$ corresponding to $\mathcal{I}_n$ only. In case of radar, actual ranges of different scatterers on the target scene are available. Therefore, we propose to use these ranges in defining EN. Thus, $\Delta_{nn'}$ can be defined as

$$\Delta_{nn'}^{\text{EN}} \triangleq \left\|\begin{pmatrix} x_n \\ x_{n'} \end{pmatrix} - \begin{pmatrix} y_n \\ y_{n'} \end{pmatrix}\right\|_2 \quad (18)$$

where (x_n, y_n) and $(x_{n'}, y_{n'})$ correspond to spatial locations of vertices $[\mathbf{s}]_n$ and $[\mathbf{s}]_{n'}$, respectively. Comparing (17) and (18), we can see that the adjacency matrix $\mathbf{W}$ needs to be updated for each sub-aperture due to the former, whereas, $\mathbf{W}$ is calculated only once, due to the latter.

Computational Complexity. The computational complexity of a standard ADMM based FLASSO for L sub-apertures is, $\mathcal{C}^{\text{FLASSO}} = \mathcal{O}(LI^{\text{FL}}N^2)$ [28], where I^{FL} denotes the number of iterations. Now, the computational complexity of updating $\mathbf{W}$ in NLTV is, $\mathcal{O}(LN^2)$. Thus, the computational complexity of GFL-NLTV is, $\mathcal{C}^{\text{GFL-NLTV}} = \mathcal{O}(LI^{\text{NL}}N^2 + LN^2)$, where I^{NL} denotes the total number of iterations. In case of ENTV, the computational complexity of updating $\mathbf{W}$ is, $\mathcal{O}(N^2)$, which is already less than NLTV. Nonetheless, the weights in ENTV are computed off-line and they do not add to the run-time complexity. Thus the computational complexity of GFL-ENTV can be written as, $\mathcal{C}^{\text{GFL-ENTV}} = \mathcal{O}(LI^{\text{EN}}N^2)$ where I^{EN} denotes the total number of iterations. Thus, we can see that the computational complexity of GFL-ENTV is comparable to FLASSO but much less than GFL-NLTV.

IV. EXPERIMENTAL RESULTS

For experiments, we consider the dataset of a backhoe target [29]. The dataset has been synthetically generated as a dome

---

[1]Note, in the case of complex valued signals, some authors, e.g., [26], suggest fusing/smoothing only the magnitude part out, instead of both real and imaginary parts, since the phase is assumed to be random [27]. However, in our view, the random phase is a constraint of the measurement system and not necessarily a requirement of fusing complex values. Therefore, in the present paper, we fuse both the real and imaginary parts. Future extensions of the work may include the random phase constraints as well.

over the target at an elevation angle of $30°$, for the angular range $\theta \in [-10°, 100°]$, with a bandwidth of 5.9 GHz centred at a frequency of 10 GHz. Figure 2a shows the target. We divide the complete angular range into $L = 22$ sub-apertures where each lth sub-aperture covers an angular range of $5°$ comprising of $K = 70$ angular samples. Instead of using the complete frequency bandwidth, we restrict ourselves to a bandwidth of 0.5 GHz which generates $M = 44$ frequency samples and a range resolution of 0.3 m. We reconstruct the target scene as an equidistant grid of 128×128 cells/pixels, which generates $N = 16384$ spatial image samples. We compare the performance of a number of methods for SAR imaging. In this respect, we reconstruct the target scene for each sub-aperture and then use (4) to construct the final image. Note, the maximum intensity value in all images has been normalised to unity and a common threshold has been applied to make the smaller values zero.

The most common method of SAR imaging is back-projection (BP) [3]. Since the signal model (1) maps the spatial locations directly into the measurements, a BP solution essentially reduces to a matched filtering solution. Figure 2b shows the result of BP based imaging. We also consider the method of [30] for comparison. For a fair comparison, we consider an ℓ_1-norm in [30] for both element-wise sparsity as well as the fusion. This essentially makes the method of [30] the same as FLASSO. Figure 2c shows the result of FLASSO based imaging. We also compare the performance of NLTV. For a fair comparison we have used the GFL framework, i.e., (11)-(15). The weights of the adjacency matrix have been obtained via (17) in (16). Parameter D in (16) has been selected so that the neighbourhood search window for each pixel is 21×21 and set $\mathcal{I}_n$ in (17) has been designed to represent indices of a 3×3 image patch centred around the nth pixel. For each sub-aperture, we use a BP based image as an estimate of $\mathbf{s}$ in (17). Figure 2d shows the result of GFL-NLTV based imaging. For GFL-ENTV, the weights of the adjacency matrix have been obtained via (18) in (16). These weights are considered fixed for all of the sub-apertures. Note, the spatial parameters of the Gaussian kernel are the same as GFL-NLTV. The SAR image is obtained by iterating over (11)-(15). Figure 2e shows the result of GFL-ENTV based imaging. Thus far, we have considered $J = M$ (see (3)). Note, even then, (3) reprsents an under-determined system of equations, in the context of our experimental setup, since $KJ < N$. We show the performance of GFL-ENTV with a reduced number of randomly selected frequency samples, i.e., $J < M$. Figure 2f shows the result of GFL-ENTV based imaging with 50% (i.e., $J = 0.5M$) of frequency samples. Note, for all of the above methods (except for BP), an update tolerance of 10^{-4} has been used as a stopping criterion for the iterations. This resulted in the average iterations of, $I^{\text{FL}} = 576$ (for FLASSO), $I^{\text{NL}} = 1344$ (for GFL-NLTV) and $I^{\text{EN}} = 237$ (for GFL-ENTV), for each sub-aperture.

Comparison of Spatial Resolution. We can see in Figure 2b for BP that different scatterers are smeared with each other, causing a reduced spatial resolution. However, the performance of all other methods is quite reasonable. To quantify the performance, we use the metric of 3 dB main-lobe width

TABLE I: Comparison of Main-Lobe Width

	20 Strongest Scatterers	40 Strongest Scatterers
BP	0.3024 m	0.306 m
FLASSO	0.1824 m	0.1682 m
GFL-NLTV	0.1530 m	0.1656 m
GFL-ENTV	0.1476 m	0.1506 m
GFL-ENTV (50%)	0.1566 m	0.1566 m

TABLE II: Comparison of Denoising Performance

	Top 30 Rows	Bottom 30 Rows
BP	16.42 dB	13.04 dB
FLASSO	6.36 dB	6.00 dB
GFL-NLTV	6.40 dB	6.86 dB
GFL-ENTV	2.78 dB	2.74 dB
GFL-ENTV (50%)	3.99 dB	3.94 dB

(MLW) [31]. MLW is a relative parameter of spatial resolution. To estimate MLW, we focus on the strong scatterers. The idea is to find a nearest point 3 dB below the value of the strong scatterer and then averaging for all the strong scatterers. A fine estimate is then obtained via interpolation over the pixels. Note, generally, strong scatterers are chosen by finding the maximum intensity point in each row/column of the image and the nearest point 3 dB below the maximum value is also found in the same row/column. However, in this paper, we prefer 2-D processing, i.e., we choose a number of strong scatterers in the image and then for each strong scatterer we find the nearest point 3 dB below the maximum value in a 2-D search (i.e., including vertical, horizontal and diagonal points), for a better estimate. Table I provides a comparison of MLW estimates for different methods, for 20 and 40 strongest scatterers, respectively. We can see, in comparison to BP, all the methods have improved resolution. However, our proposed method outperforms all other methods. The performance of GFL-NLTV is quite close. Nonetheless, it has been achieved at a substantially higher computational complexity. We can also see, despite a reduction in frequency samples by 50%, GFL-ENTV (50%) shows substantial gain in spatial resolution.

Comparison of Denoising. In order to show the denoising performance of our proposed algorithm, we use the parameter of standard deviation of a smooth patch of the dB-valued target image. Table II shows the denoising performance for top 30 and bottom 30 rows of the target image, respectively. We can see, our proposed method considerably outperforms all other methods. Even GFL-ENTV (50%) also shows substantial gain.

V. CONCLUSIONS

In this paper, we have proposed graph based SAR imaging for improved spatial resolution and denoising. We have proposed the concept of extended neighbourhood to account for the irregularity of SAR spatial grid and the nonuniformity of reflectivity field. We solve our optimisation problem via ADMM. Our proposed method has reduced computational

(a) Backhoe target

(b) BP

(c) FLASSO

(d) GFL-NLTV
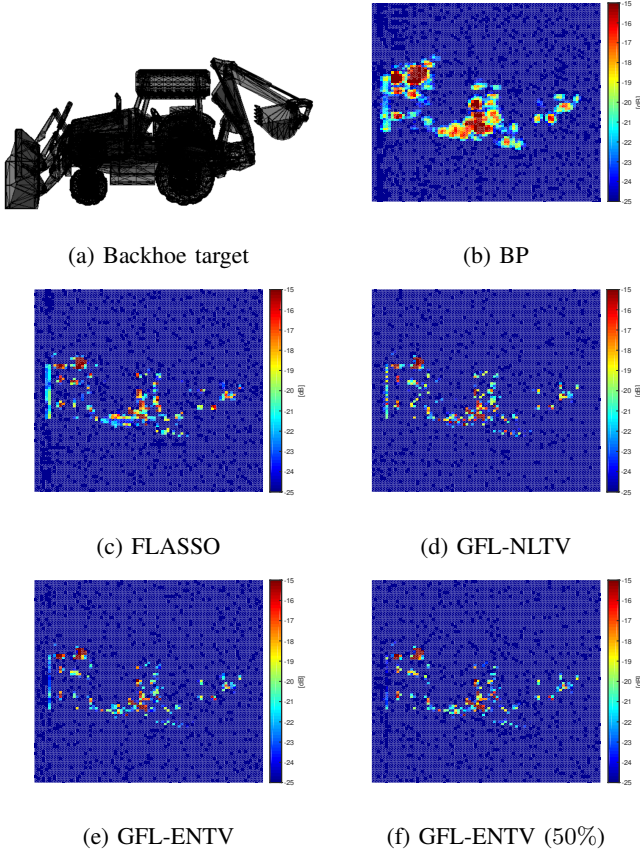
(e) GFL-ENTV

(f) GFL-ENTV (50%)

Fig. 2: Performance Comparison of SAR Imaging Techniques

complexity and enhanced spatial resolution and denoising. Experimental results prove that our proposed method outperforms a number of SAR imaging techniques, including the patch based nonlocal method.

REFERENCES

[1] W. Carrara, R. Goodman, and R. Majewski, *Spotlight Synthetic Aperture Radar*. Boston: Artech House, 1995.
[2] C. Jakowatz, D. Wahl, P. Eichel, D. Ghiglia, and P. Thompson, *Spotlight-Mode Synthetic Aperture Radar: A Signal Processing Approach*. MA, USA: Kulwer Academic Publishers, 1996.
[3] M. Soumekh, *Synthetic Aperture Radar Signal Processing with MATLAB Algorithms*. NY, USA: John Wiley & Sons, Inc., 1999.
[4] M. Cetin, I. Stojanovic, O. Onhon, K. Varshney, S. Samadi, W. C. Karl, and A. S. Willsky, "Sparsity-driven synthetic aperture radar imaging: Reconstruction, autofocusing, moving targets, and compressed sensing," *IEEE Signal Processing Magazine*, vol. 31, no. 4, pp. 27–40, July 2014.
[5] D. I. Shuman, S. K. Narang, P. Frossard, A. Ortega, and P. Vandergheynst, "The emerging field of signal processing on graphs: Extending high-dimensional data analysis to networks and other irregular domains," *IEEE Signal Processing Magazine*, vol. 30, no. 3, pp. 83–98, May 2013.
[6] A. Sandryhaila and J. M. F. Moura, "Discrete signal processing on graphs," *IEEE Transactions on Signal Processing*, vol. 61, no. 7, pp. 1644–1656, April 2013.
[7] G. Cheung, E. Magli, Y. Tanaka, and M. K. Ng, "Graph spectral image processing," *Proceedings of the IEEE*, vol. 106, no. 5, pp. 907–930, May 2018.
[8] M. Belkin and P. Niyogi, "Laplacian eigenmaps for dimensionality reduction and data representation," *Neural Comput.*, vol. 15, no. 6, pp. 1373–1396, Jun. 2003.
[9] R. Tibshirani, M. Saunders, S. Rosset, J. Zhu, and K. Knight, "Sparsity and smoothness via the fused LASSO," *Journal of the Royal Statistical Society Series B*, pp. 91–108, 2005.
[10] S. Gishkori, L. Daniel, M. Gashinova, and B. Mulgrew, "Imaging for a forward scanning automotive synthetic aperture radar," *IEEE Transactions on Aerospace and Electronic Systems*, p. to appear, 2018.
[11] L. I. Rudin, S. Osher, and E. Fatemi, "Nonlinear total variation based noise removal algorithms," *Phys. D*, vol. 60, no. 1-4, pp. 259–268, Nov. 1992.
[12] A. Buades, B. Coll, and J. M. Morel, "A review of image denoising algorithms, with a new one," *Multiscale Modeling & Simulation*, vol. 4, no. 2, pp. 490–530, 2005.
[13] G. Gilboa and S. Osher, "Nonlocal operators with applications to image processing," vol. 7, pp. 1005–1028, 01 2008.
[14] Y. Lou, X. Zhang, S. Osher, and A. Bertozzi, "Image recovery via nonlocal operators," *Journal of Scientific Computing*, vol. 42, no. 2, pp. 185–197, Feb 2010.
[15] C. Deledalle, L. Denis, and F. Tupin, "Iterative weighted maximum likelihood denoising with probabilistic patch-based weights," *IEEE Transactions on Image Processing*, vol. 18, no. 12, pp. 2661–2672, Dec. 2009.
[16] H. Zhong, Y. Li, and L. Jiao, "SAR image despeckling using bayesian nonlocal means filter with sigma preselection," *IEEE Geoscience and Remote Sensing Letters*, vol. 8, no. 4, pp. 809–813, Jul. 2011.
[17] C. Deledalle, L. Denis, G. Poggi, F. Tupin, and L. Verdoliva, "Exploiting patch similarity for SAR image processing: The nonlocal paradigm," *IEEE Signal Processing Magazine*, vol. 31, no. 4, pp. 69–78, Jul. 2014.
[18] S. Boyd, N. Parikh, E. Chu, B. Peleato, and J. Eckstein, "Distributed optimization and statistical learning via the alternating direction method of multipliers," *Found. Trends Mach. Learn.*, vol. 3, no. 1, pp. 1–122, Jan. 2011.
[19] D. P. Bertsekas and J. N. Tsitsiklis. Parallel and Distributed Computation: Numerical Methods, 1997.
[20] D. L. Donoho, "Compressed sensing," *IEEE Transactions on Information Theory*, vol. 52, no. 4, April 2006.
[21] E. Candes, J. Romberg, and T. Tao, "Robust uncertainty principles: exact signal reconstruction from highly incomplete frequency information," *IEEE Transactions on Information Theory*, vol. 52, no. 2, pp. 489–509, Feb. 2006.
[22] V. M. Patel, G. R. Easley, J. D. M. Healy, and R. Chellappa, "Compressed synthetic aperture radar," *IEEE Journal of Selected Topics in Signal Processing*, vol. 4, no. 2, pp. 244–254, April 2010.
[23] R. Moses, L. Potter, and M. Cetin, "Wide-angle SAR imaging," *Proc.SPIE*, vol. 5427, pp. 164–175, 2004.
[24] J. Fang, Z. Xu, B. Zhang, W. Hong, and Y. Wu, "Fast compressed sensing SAR imaging based on approximated observation," *IEEE Journal of Selected Topics in Applied Earth Observations and Remote Sensing*, vol. 7, no. 1, pp. 352–363, Jan 2014.
[25] K. Aberman and Y. C. Eldar, "Sub-Nyquist SAR via Fourier domain range-Doppler processing," *IEEE Transactions on Geoscience and Remote Sensing*, vol. 55, no. 11, pp. 6228–6244, Nov 2017.
[26] M. Cetin and W. C. Karl, "Feature-enhanced synthetic aperture radar image formation based on nonquadratic regularization," *IEEE Transactions on Image Processing*, vol. 10, no. 4, pp. 623–631, Apr 2001.
[27] D. C. Munson and J. L. C. Sanz, "Image reconstruction from frequency-offset fourier data," *Proceedings of the IEEE*, vol. 72, no. 6, pp. 661–669, Jun. 1984.
[28] B. Wahlberg, S. Boyd, M. Annergren, and Y. Wang, "An ADMM algorithm for a class of total variation regularized estimation problems," *IFAC Proceedings Volumes*, vol. 45, no. 16, pp. 83 – 88, 2012, 16th IFAC Symposium on System Identification.
[29] K. Naidu and L. Lin, "Data dome: full k-space sampling data for high-frequency radar research," *Proc.SPIE*, vol. 5427, pp. 200 – 207, 2004.
[30] M. Cetin, W. C. Karl, and D. A. Castanon, "Feature enhancement and ATR performance using nonquadratic optimization-based SAR imaging," *IEEE Transactions on Aerospace and Electronic Systems*, vol. 39, no. 4, pp. 1375–1395, Oct 2003.
[31] G. R. Benitz, "High-definition vector imaging," in *Lincoln Laboratory Journal*, vol. 10, no. 2, 1997, pp. 147–170.